

# Physicochemical Properties and Release Study of Antimetabolite-Incorporated Stearoyl Chitosan

Anita Marlina\* and Misni Misran

Cite This: *ACS Omega* 2023, 8, 40494–40507

Read Online

ACCESS |



Metrics &amp; More



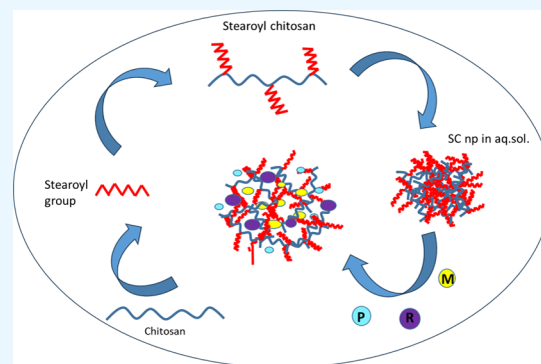
Article Recommendations



Supporting Information

**ABSTRACT:** Stearoyl chitosan (SC), derived from the acylation of chitosan, contributes to the efficiency of drug delivery systems because of its structure, which accommodates the drug in a particle. Nonetheless, its role in chemotherapy has been largely unexplored. The present study involves the synthesis of stearyl chitosan through the reaction of depolymerized chitosan with stearyl chloride under mild reaction conditions. The resulting compound was subjected to structural analysis utilizing Fourier-transform infrared (FTIR) spectroscopy,  $^1\text{H}$  NMR, and X-ray diffraction (XRD) spectroscopy. The dispersion of SC molecules in phosphate-buffered saline (PBS) forms SC nanoparticles. The best dispersion of SC in the solution was achieved at a 1:60 chitosan-to-stearyl chloride weight ratio. Three antimetabolite drugs, methotrexate, pemetrexed, and raltitrexed, were selected to examine the loading efficacy of SC.

Pemetrexed had the highest drug-loading value of 36.8% among the three antimetabolites incorporated into SC, along with an encapsulation efficiency of 85.1%. The size of SC loaded with antimetabolites ranged from 225 to 369 nm, and their spherical form was verified via a transmission electron microscope. The *in vitro* release study showed that SC demonstrated controlled drug release, suggesting that SC nanoparticles have significant promise as a delivery strategy for chemotherapy.



## 1. INTRODUCTION

Categorized as chemotherapeutic drugs, antimetabolites mitigate the propagation of cancer cells by hindering their ability to copy DNA and RNA.<sup>1,2</sup> Rapid tumor progression, as observed in leukemia, breast, ovarian, and gastrointestinal cancer types, demands this type of antimetabolite medication.<sup>3</sup> The molecular structure of an antimetabolite comprises a cluster of purines or pyrimidines, nucleotides that function as reactants, and other components related to metabolic pathways.<sup>4</sup> Nevertheless, there are certain limitations associated with the utilization of antimetabolites in the context of cancer therapy, whereby cancer cells may gradually acquire resistance to antimetabolites.<sup>5</sup> On the other hand, antimetabolite medications are toxic to the liver, kidneys, and bone marrow, and they cause side effects and are not selective to the target cells.<sup>6</sup> This has led scientists to investigate novel strategies for administering antimetabolites with selective targeting capabilities.

The technological efficiency of antimetabolite delivery systems has attracted considerable attention from scientists. Recent studies concerning antimetabolite encapsulation have investigated 5-fluorouracil encapsulation in B40 fullerene,<sup>7</sup> single-walled carbon nanotubes,<sup>8</sup> magnetically responsive microbubbles,<sup>9</sup> and gold nanoparticles.<sup>10</sup> Furthermore, methotrexate has been studied in poly(lactic-co-glycolic acid) (PLGA) nanoparticles<sup>11</sup> and deoxycholate-D- $\alpha$ -tocopheryl polyethylene.<sup>12</sup> A new study was conducted by Li et al. to

design a long-acting drug delivery system of intraocular lenses to encapsulate methotrexate for posterior capsule opacification prophylaxis.<sup>13</sup> All of the aforementioned carriers exhibited either sustained or controlled drug release via both oral and intravenous administration routes.

Chitosan and its derivatives have been extensively examined and deployed as efficient drug carriers owing to their interesting properties, such as nontoxicity, biocompatibility, biodegradability, bioadhesiveness, antimicrobial, and antifungal.<sup>14–20</sup> Studies pertaining to chitosan and its modified forms for drug delivery systems have demonstrated sustained release and colon-targeting delivery systems.<sup>21–24</sup> Drug carriers derived from acylated chitosan, ranging from short chain to long chain, have been widely utilized in many applications, including nanoparticle formulations and as coatings for liposomes.<sup>25–27</sup> The hydrophobicity increases proportionally with the length of the chain, thereby facilitating the encapsulation of the lipophilic medication.

Received: July 18, 2023

Accepted: October 6, 2023

Published: October 20, 2023



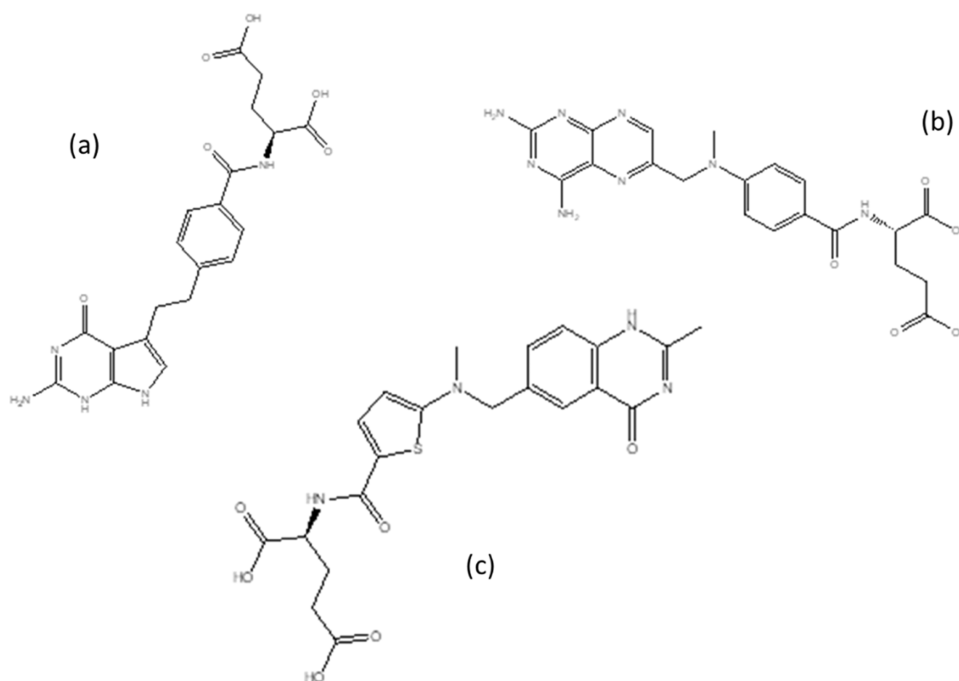


**Figure 1.** Antimetabolite drugs: (a) pemetrexed, (b) methotrexate, and (c) raltitrexed.

**Table 1.** Chemical Properties of Antimetabolites

antimetabolite	chemical formula	log <i>P</i> (oct/water)	solubility in PBS (mg·mL <sup>-1</sup> )	drug delivery aystem	molecular weight (gmol <sup>-1</sup> )
pemetrexed (P)	C <sub>20</sub> H <sub>21</sub> N <sub>5</sub> O <sub>6</sub>	1.52	10	gold nanoparticle <sup>34</sup>	597.5
methotrexate (M)	C <sub>20</sub> H <sub>19</sub> H <sub>3</sub> N <sub>8</sub> O <sub>5</sub>	-0.11	1	biodegradable mesoporous silica nanoparticles; <sup>35</sup> hyaluronic acid-mangiferin-methotrexate nanodrug; <sup>36</sup> microneedle patch <sup>37</sup>	457.5
raltitrexed (R)	C <sub>21</sub> H <sub>22</sub> N <sub>4</sub> O <sub>6</sub> S	-0.82	<0.043	raltitrexed combined with gold and silver nanoparticles; <sup>38</sup> drug-eluting beads (DEB-TACE) <sup>39</sup>	458.5

To date, studies on stearyl chitosan with a C18 chain length as a drug delivery system have been limited. According to Chirio et al., nanoparticles of stearyl chitosan (SC) loaded with curcumin generated from the microemulsion cold dilution method demonstrated mean diameters ranging at 200–250 nm and 73% of curcumin entrapment efficiency.<sup>28</sup> Meanwhile, fish oil incorporated into *N*-stearyl *O*-butylglyceryl chitosan resulted in a 12.9 μm size distribution and -101.4 mV ζ-potential.<sup>29</sup> Liu et al. introduced an amphiphilic carrier by grafting chitosan with stearyl chloride and poly(vinylpyrrolidone) (PVP). The distribution size of paclitaxel-loaded PVP-SC was 144 nm with -7.5 mV ζ-potential.<sup>30</sup> In another study, Yang et al. reported that the paclitaxel was successfully encapsulated into *L*-Carnitine-conjugated chitosan-stearic acid polymer micelles with 157.1 nm particle size and 15.96% loading capacity.<sup>31</sup>

In the present study, a delivery system was synthesized using the self-assembly of stearyl chitosan to integrate three antimetabolites with varying log *P* values, specifically pemetrexed, methotrexate, and raltitrexed, as shown in Figure 1. The acylation process involves the reaction of depolymerized chitosan with stearyl chloride under mild conditions, which is facilitated by an acidic environment that enhances the rate of acylation. The optimal formulation of stearyl chitosan was employed to encapsulate antimetabolites using the solvent evaporation-hydration technique.<sup>32</sup> Therefore, the objective of this work was to assess the most stable formulation of

stearyl chitosan based on its physicochemical properties. Additionally, the incorporation of antimetabolite into the selected stearyl chitosan was investigated by analyzing the encapsulation efficiency, particle size, ζ-potential, morphology, and in vitro release. The three antimetabolites were used as model drugs based on variations in log *P* values, as presented in Table 1. The log *P* value was calculated empirically by dividing the chemical between presaturated octanol and water phases in a shake flask.<sup>33</sup> It is hypothesized that pemetrexed, exhibiting a positive value, demonstrates a tendency to readily engage with the hydrophobic moiety of stearyl compared to methotrexate and raltitrexed. Consequently, this interaction is anticipated to yield a high encapsulation value and sustained release behavior. In addition, stearyl chitosan is most likely to be a suitable delivery system with a controlled release dosage form for these antimetabolites because of its narrow therapeutic index. To the best of our knowledge, there are no reports documenting the effects of stearyl chitosan on encapsulated drugs with different lipophilicity values.

## 2. EXPERIMENTAL SECTION

**2.1. Materials.** The compounds used in this study were purchased commercially and used as received without further purification. Chitosan (*M<sub>w</sub>* 100,000–300,000 Da) was bought from Sigma-Aldrich. Sodium hydroxide (NaOH) and NaNO<sub>2</sub> were obtained from Fluka (Switzerland). Ethanol, hydrochloric acid, chloroform, acetone, deuterium oxide (D<sub>2</sub>O), deuterated

acetic acid (CD<sub>3</sub>COOD), and tetrahydrofuran (THF) were purchased from Merck (Germany). Methotrexate, pemetrexed, and raltitrexed were purchased from Cayman Chemicals.

**2.2. Synthesis of Stearoyl Chitosan.** A chitosan solution (1% w/v) was prepared by dissolving chitosan (DD 85%) in a 1% v/v acetic acid solution and stirring at 80 °C for 6 h. Prior to the acylation procedure, water-soluble chitosan was obtained by depolymerizing chitosan with NaNO<sub>2</sub>.<sup>40</sup> 10 mL of NaNO<sub>2</sub> was introduced into the neutralized chitosan solution, followed by agitation of the resulting mixture at a temperature of 30 °C for 1 h. The pH of the solution was adjusted to 8 to form a suspension containing insoluble chitosan. Water-soluble chitosan was precipitated via filtration and centrifugation. Subsequently, the chitosan, designated as NC, was subjected to a drying process in a vacuum oven to facilitate analysis.

The synthesis of stearoyl chitosan involves the introduction of stearoyl chloride into a solution of depolymerized chitosan (NC). The solution was prepared using the same methodology described previously using a 1% w/v acetic acid solution. In this synthesis, acetic acid was utilized not only to dissolve the depolymerized chitosan but also to accelerate the acylation process, similar to the function of a Lewis acid catalyst. The acylation was performed at 30 °C for 5 h. Different weight ratios of stearoyl chloride were introduced into the chitosan solution with continuous stirring. Based on the glucosamine fraction in chitosan, the weight ratios of chitosan to stearoyl chloride were set as follows: 1:20, 1:40, 1:60, 1:80, and 1:100, and labeled as SC1, SC2, SC3, SC4, and SC5, respectively. The resultant mixture was agitated for 5 h at a controlled temperature of 30 °C using a Lauda Ecoline RE207 water bath to produce a homogeneous solution. After optimization of the acylation process, the solution was left overnight. An equivalent volume of acetone was added to the mixture to form a suspension. The precipitated SC was isolated from the unreacted stearoyl chloride via centrifugation for 15 min at 5000 rpm. Finally, SC was retrieved by drying the precipitate for 12 h in a vacuum oven.

**2.3. Preparation of Self-Assembled Stearoyl Chitosan Nanoparticles.** In this study, nanoparticles were formed when stearoyl chitosan (SC) was allowed to self-assemble in aqueous solutions of various concentrations. First, each SC (0.5 mg) was solubilized in 5 mL of tetrahydrofuran (THF). A volume of 10 mL of phosphate-buffered saline (PBS) with a concentration of 0.01 M and pH 7.4 was gradually introduced into the prepared SC solution. The mixture was sonicated for 1 h at a rotational speed of 300 rpm to facilitate the self-assembly of the SC into nanoparticles. Subsequently, THF was removed using a rotary evaporator by heating the mixture to 50 °C. Nitrogen gas was then introduced into the solution afterward in order to purge any residual THF. PBS, with a pH of 7.4, was employed during the preparation of the self-assembled SC to enhance its resemblance to the pH of human blood. Moreover, the use of isotonic PBS can mitigate the occurrence of osmotic stress on stearoyl chitosan during self-assembly.

**2.4. Fourier Transform Infrared (FTIR) Spectroscopy.** Attenuated total reflectance (GladiATR) FTIR spectroscopy (Pike Technologies) was employed to identify the functional groups of native chitosan (NC) and SC. All measurements were performed in the range 4000–550 cm<sup>-1</sup> with 32 scans and a resolution of 4 cm<sup>-1</sup>.

The degree of substitution of SC was controlled by the weight ratio (chitosan to stearoyl chloride) and calculated using the following equation

$$DS = 1 - DD \quad (1)$$

Degree of substitution (DS) and DD refer to the degree of substitution and the degree of deacetylation, respectively.<sup>25</sup> The value of DD was determined based on the ratio of  $A_{1655}/A_{3450}$ , as given in the equation below<sup>41</sup>

$$DD (\%) = \left( \frac{A_{1655}}{A_{3450}} \times \frac{100}{1.33} \right) \quad (2)$$

where  $A_{1655}$ ,  $A_{3450}$ , and 1.33 correspond to absorbance values at 1655 cm<sup>-1</sup> due to C=O (amide I), band at 3450 cm<sup>-1</sup> owing to the O–H band, and the assumption for fully deacetylated chitosan,<sup>42</sup> respectively.

**2.5. <sup>1</sup>H Nuclear Magnetic Resonance (<sup>1</sup>H NMR).** NMR spectroscopy (Bruker, Avance III 400 MHz) was used to determine the number of protons in the NC and various SCs. <sup>1</sup>H NMR analysis was performed by dissolving the samples in 2% CD<sub>3</sub>COOD and D<sub>2</sub>O solutions. To increase the solubility of SC, all of the samples were measured at 70 °C. Delta NMR data processing software was used to analyze the NMR spectra.

**2.6. Powder X-ray Diffraction Analysis.** The diffraction patterns of the NC and SC powders were captured using a PANalytical powder X-ray diffractometer (EMPYREAN) with a Cu X-ray source (Cu K- $\alpha$ ) in reflectance mode (wavelength: 0.15418 nm and 2 $\theta$ : 4–40°). HighScore Plus software was used to analyze the diffractograms.

**2.7. Determination of Water Solubility Using UV–Visible Spectroscopy.** The water solubility of SC was determined by using an ultraviolet–visible (UV–vis) spectrophotometer. A saturated sample of each SC was prepared in deionized water and agitated for 1 h at 30 °C. Subsequently, the UV–visible absorbance of the saturated SC solution was measured. A saturated SC solution, which served as a stock solution, was subsequently employed to produce a series of SC solutions at known concentrations. A calibration curve was established by plotting the absorbance of a series of SC solutions at a wavelength of 271 nm against their concentration. The water solubility of each SC sample was calculated by extrapolating the saturated SC value obtained from the calibration curve.

**2.8. Determination of Critical Micelle Concentration (CMC).** The critical micelle concentration of various SCs was determined using an Eutech Conductivity Meter CyberScan CON 510. A series of concentrated SC was prepared in deionized water, and its conductivity was then assessed. The critical micelle concentration (CMC) is the concentration at which the linear relationship between the conductivity and the surfactant concentration breaks down.

**2.9. Determination of Average Molecular Weight.** The static light scattering technique was employed in this study to determine the average molecular weight of NC and various SC ratios using a Zetasizer Nano (Malvern Instruments). Samples of various concentrations were dispersed in an aqueous solution. The measurements were repeated three times to determine the data accuracy. Debye plots of intensity against concentration were plotted to calculate the average molecular weight based on the intercept using the following equation

$$\frac{KC}{R_\theta} = \frac{1}{M_w} + 2A_2C \quad (3)$$

The concentration-dependent  $KC/R_\theta$  linear fit (the Debye plot) showed an intercept equivalent to the inverse of molecular weight ( $M_w$ ) and a slope equivalent to the second virial coefficient ( $A_2$ ). The Rayleigh ratio, denoted as  $R_\theta$ , is utilized to determine the ratio of the intensity of scattered light to the intensity of incident light at a specific angle  $\theta$ . Additionally,  $C$  is the sample concentration and  $K$  is the Debye constant.

**2.10. Particle Size and  $\zeta$ -Potential Analyses.** The dynamic light scattering method was applied to measure the hydrodynamic diameters of NC and SC using a Zetasizer Nano ZS (Malvern Instruments, U.K.) with a backscatter detection of  $173^\circ$ . In contrast, the  $\zeta$ -potentials of NC and SC were measured at a detection angle of  $17^\circ$ . All measurements were performed in triplicate in an aqueous solution at  $25^\circ\text{C}$ .

**2.11. Morphology Analysis.** The morphology of the SC nanoparticles incorporated into antimetabolites was assessed in this study using an LEO Libra-120 transmission electron microscope (TEM; Carl Zeiss, Germany) with an accelerating voltage of 120 kV. Briefly, a drop of SC dispersion was deposited on a carbon-coated copper grid and dried for 3 min at room temperature. Next, a drop of 1% (w/v) phosphotungstic acid (PTA) was employed to stain the specimen. The grid was then gently transferred to a desiccator and dried for 24 h.

**2.12. Encapsulation Efficiency and Loading Capacity of Drugs.** The three antimetabolites encapsulated in SC in this study were pemetrexed, methotrexate, and raltitrexed. Each drug was individually encapsulated in the selected SC, based on its optimal physicochemical properties, as a colloidal system. Various weight ratios of the drug to carrier and SC solution were prepared in PBS (0.01 M, pH 7.4). SC (1 mg) was loaded with 0.025–0.125 mg of various drugs to yield a 10 mL suspension. The encapsulation of different drugs into the SC was accomplished in the same manner as the self-assembly of the SC nanoparticles. After the SC and each drug were dissolved in THF separately, the two solutions were mixed using an orbital shaker and agitated for 30 min. A solution of 0.01 M phosphate-buffered saline (PBS) (pH 7.4) was introduced into the mixture of SC and the drug. Subsequently, the mixture was agitated at 300 rpm for 24 h on an orbital shaker. Finally, THF was extracted by using a rotating evaporator and nitrogen gas. To separate the free drug, 1 mL of the sample was run through a centrifugal concentrator (Vivaspin 6) with a pore size of 10 kDa molecular weight cutoff (MWCO). Centrifugation was performed for 15 min at 5000 rpm. A Varian Cary 50 UV–vis spectrophotometer was used to analyze the free drug concentration at the bottom of the centrifugal concentrator. Methotrexate, pemetrexed, and raltitrexed exhibited maximum wavelengths of 373, 225, and 351 nm, respectively. All assays were performed in triplicate. The encapsulation efficiency was calculated by using the following equation<sup>32</sup>

$$EE (\%) = \frac{(\text{total drug added} - \text{free drug})}{\text{total drug added}} \times 100\% \quad (4)$$

Drug loading was calculated in this study. In brief, drug loading refers to the fraction of drug found in a nanoparticle based on the total amount of drug applied while preparing the nanoparticle yield.<sup>47</sup>

$$DL (\%) = \frac{(\text{total drug added} - \text{free drug})}{\text{total nanoparticle}} \times 100\% \quad (5)$$

**2.13. In Vitro Release Study.** In this study, a Franz cell diffusion system (Hanson Research Co.) was used to perform an in vitro antimetabolite release. The system consisted of six glass cells, a 4 mL receptor chamber, a programmable circulator bath, and a Hanson Microette Plus Autosampler. A regenerated cellulose membrane with 5 kDa of MWCO (63 mm, Nest Group Inc.) was placed onto the glass cells after they were washed with deionized water and soaked for 12 h in PBS (0.01 M, pH 7.4). The experiment was carried out at  $37 \pm 0.1^\circ\text{C}$  separately for each drug. A similar sample preparation technique was used to determine the encapsulation efficiency. Each drug (0.1 mg) was incorporated into the SC nanoparticles, and the drug-loaded SC dispersion was transported into the donor chamber. Owing to the gradient concentration, the drug diffused into the receptor chamber containing PBS solution (0.01 M) through the membrane. Sampling was performed at 0.5, 1, 2, 4, 6, 8, 12, 16, 20, and 24 h, in which an aliquot of 1 mL in the receptor chamber was automatically transferred into vials (Agilent). Subsequently, the solution in the receptor chamber was gradually replaced with a fresh receiving medium of PBS (0.01 M) to maintain a constant volume. A Varian Cary 50 UV–visible spectrophotometer was used to measure the content of the studied drug at 373 nm (methotrexate), 225 nm (pemetrexed), and 351 nm (raltitrexed). A comparative analysis was performed between the cumulative drug release from the SC-encapsulated drug and the free drug release over time to identify the drug release features.

Drug release kinetics was quantitatively predicted by deploying several mathematical models and analyzing the overall release behavior. Using the DDSolver tool, the cumulative release profile of the three selected antimetabolites incorporating SC was fitted with Higuchi, first-order, and Korsmeyer–Peppas kinetic models.<sup>43</sup> The first-order kinetic model was built by calculating the cumulative fraction of drug release as a logarithm over time. In the Higuchi kinetic model, the plot reflects the cumulative drug release as a percentage of the square root of the time. Meanwhile, the Korsmeyer–Peppas kinetic model was constructed by plotting the logarithm of the percentage of cumulative drug release against the logarithm of time.

$$\text{first order model: } \ln(1 - F) = k_1 t \quad (6)$$

$$\text{higuchi model: } F = k_2 t^{1/2} \quad (7)$$

$$\text{Korsmeyer–Peppas model } \begin{cases} \bullet \frac{M_t}{M_\infty} \\ \bullet k_3 t^n \end{cases} \quad (8)$$

where  $F$  denotes the fraction of drug released at time  $t$  in both first-order and Higuchi kinetic models. In the Korsmeyer–Peppas kinetic model,  $M_t$  refers to the drug released at time  $t$ ,  $k_1$  signifies the release constant in the first order,  $k_2$  is the release constant in the Higuchi model,  $k_3$  denotes the kinetic constant,  $M_\infty$  exemplifies the amount of drug released at infinite time, and  $n$  represents the release exponent.

**2.14. Statistical Analysis.** Data were analyzed using Origin and Analysis of Variance (ANOVA). Significant variations observed between the mean values of the samples

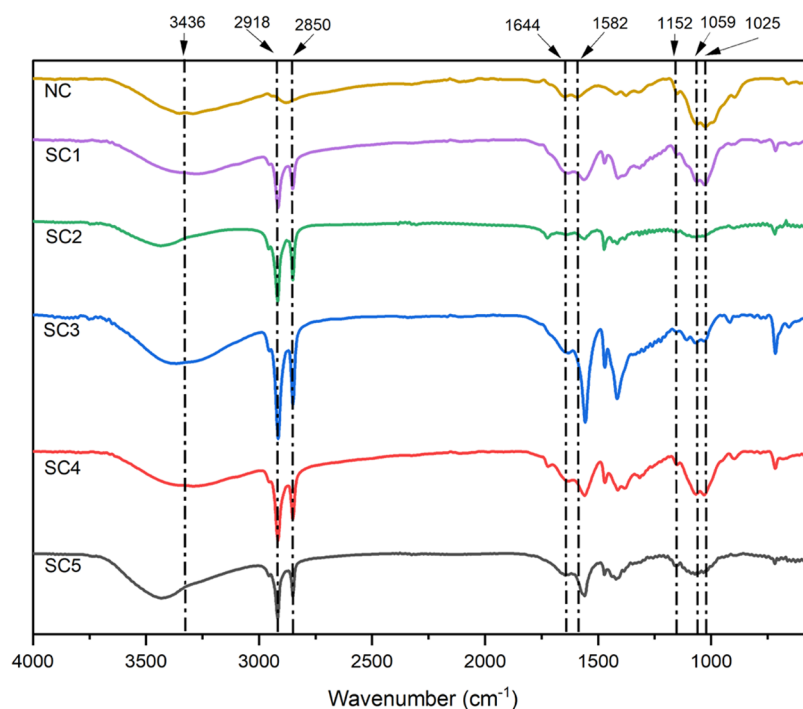


**Figure 2.** FTIR spectra of NC and stearyl chitosan (SC1–SC5).

were determined using one-way analysis of variance (ANOVA), with a significance level set at  $p < 0.05$ .

### 3. RESULTS AND DISCUSSIONS

**3.1. FTIR Analysis.** The stearyl chitosan (SC) structure was confirmed through the analysis of the FTIR spectra. Additionally, the FTIR spectra of stearyl chitosan and native chitosan were compared, as depicted in Figure 2. The NC spectrum demonstrated a broad peak at  $3436\text{ cm}^{-1}$  attributed to O–H stretching vibration, which could have overlapped with N–H stretching vibration.<sup>21</sup> The band at  $1152\text{ cm}^{-1}$  was ascribed to C–O–C stretching vibration, which reflects a  $\beta(1 \rightarrow 4)$  glycosidic linkage,<sup>44,45</sup> whereas the stretching vibration of C–O occurred at  $1059$  and  $1025\text{ cm}^{-1}$ . When examining the SC spectrum, it was observed that the O–H stretching vibration exhibited a slight shift with the exception of SC1. This discrepancy in SC1 may be attributed to its resistance or limited detection during acylation. One notable distinction is the emergence of two distinct peaks following the acylation process at  $2918$  and  $2850\text{ cm}^{-1}$ , denoted as the stretching of asymmetric and symmetric  $\text{CH}_2$ , correspondingly.<sup>46</sup> Moreover, the two prominent peaks at  $1644$  and  $1582\text{ cm}^{-1}$  denoted C=O stretching vibration (amide I) and N–H stretching vibration (amide II), respectively.<sup>21,46</sup> All SC ratios demonstrated bands similar to those of SC1. This signified that the acylation mechanism was more highly selective for amine groups than hydroxyl groups in chitosan due to the electronegativity of amines.<sup>47,48</sup> The notion is verified due to the absence of a band at  $1750\text{ cm}^{-1}$  in all SC spectra, reflecting the O-ester group.<sup>46</sup>

The encapsulation of drugs into stearyl chitosan can potentially lead to intermolecular interactions between the drug and the carrier. Figure 3 illustrates the interaction between stearyl chitosan (SC3) and methotrexate. Upon conducting a comparative analysis of the spectra of SC3, methotrexate, and M-loaded SC3, it is obvious that there is a noticeable difference in the intensity of the peaks associated

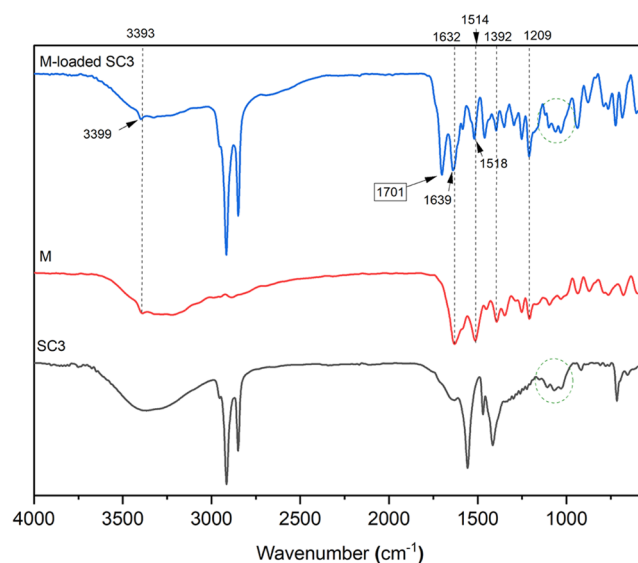


**Figure 3.** FTIR spectra of SC3, methotrexate, and M-loaded SC3.

with each functional group. In the methotrexate spectrum, a prominent and broad peak was observed at  $3393\text{ cm}^{-1}$ , which can be attributed to the vibrations of the N–H bonds. Notably, this particular peak exhibited a slight shift when methotrexate was loaded onto SC3. Shifts in the peaks in the spectral range  $1632$ – $1514\text{ cm}^{-1}$  were observed, which can be ascribed to the vibrations of C=C bonds in the aromatic ring and R-NH<sub>2</sub> groups. Additionally, the presence of peaks at  $1392$  and  $1209\text{ cm}^{-1}$  suggested the presence of stretching vibrations in the C–C or C–H bonds. The occurrence of a highly pronounced carbonyl C=O peak is likely attributable to the impact of the functional group derived from SC3, namely, the O–H group. This finding indicated that the interaction between methotrexate and the carrier molecule was due to hydrogen bonding.

**3.2.  $^1\text{H}$  NMR Analysis.** The  $^1\text{H}$  NMR spectra of NC and SC3 in deuterated acetic acid are shown in Figure 4.

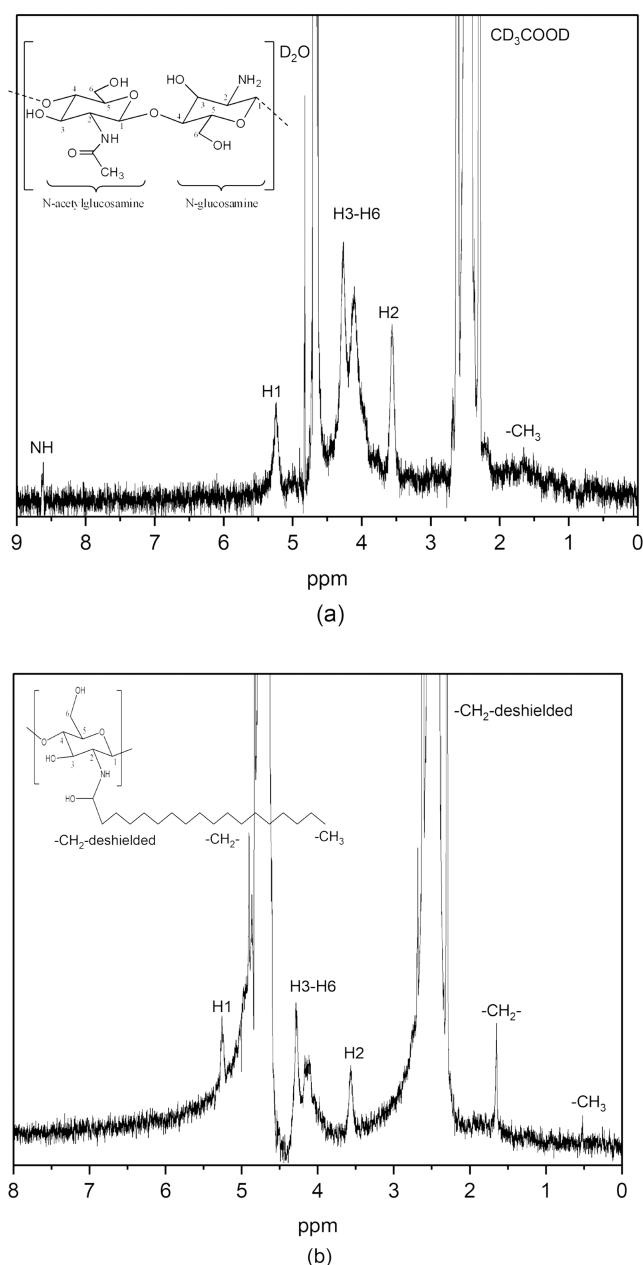


**Figure 4.**  $^1\text{H}$  NMR spectra of the (a) NC and (b) SC3.

Deuterium oxide and deuterated acetic acid exhibited chemical shifts of 4.61 and 2.03 ppm, respectively. The spectrum of chitosan revealed peaks at 1.80, 3.56, 3.91–4.33, 5.24, and 8.62

ppm attributed to  $\text{CH}_3$  (*N*-acetylglucosamine), H2, H3–H6, H1, and NH, respectively. The proton signal seen in Figure 4b is identical to that of NC, except for the  $\text{CH}_3$  (*N*-acetyl) and NH peaks, which presumably diminished owing to the presence of stearoyl. However, the effectiveness of this acylation method was evidenced by the prominent presence of stearoyl group peaks observed consistently over subsequent ranges. Several stearoyl moiety peaks were found in the ranges 0.61–1.55, 1.73, 2.20, 2.28, and 2.55, 2.57 ppm assigned to methyl protons  $\text{R}-\text{CH}_3$ , methylene protons  $\text{R}-\text{CH}_2-\text{CH}_3$ , methylene protons  $\text{R}-\text{CH}_2-\text{CH}_2-\text{CH}_3$ , and methylene protons  $\text{R}-\text{CH}_2-\text{C}=\text{O}$ , respectively. The same spectrum was recorded for SC1, SC2, SC4, and SC5, with varying intensities.

**3.3. Average Molecular Weight, Water Solubility, and Critical Micelle Concentration.** The average molecular weights of various SCs are listed in Table 2. After depolymerization of medium molecular weight chitosan using sodium nitrite, the molecular weight of the new chitosan (NC) was found to be 17 kDa. The introduction of a stearoyl moiety into the NC gradually increased the average molecular weight based on the amount of stearoyl. The highest average molecular weight of 57 kDa was observed in SC5, where the weight ratio of chitosan to stearoyl was 1:100 based on the *N*-glucosamine unit. As shown in the table, the substitution of a hydrogen atom with a stearoyl is energetically favorable, such that the acylation process occurs spontaneously. Although there is no direct relationship between the average molecular weight and degree of substitution, these two parameters affect the solubility of SC in deionized water. As the NC was acylated, the water solubility decreased significantly owing to the length of the side chain. The more stearoyl was added, the less soluble the SC was in deionized water.

The critical micelle concentration (CMC) of soluble SC was determined by using conductivity measurements. This method allows the observation of the formation of micelles or self-aggregation of SC.<sup>49</sup> At low concentrations, SC appears as individual polymer chains with a charge capable of conducting current. As the concentration increased, the self-assembly of SC molecules occurred, leading to the formation of micelles. At this concentration, the flow of electrical current through water is hindered by the production of micelles. This phenomenon gives rise to discontinuities or fractures in the system, where the conductivity initially exhibits a linear increase with increasing concentration. When the concentration of SC is high, agglomerates are formed, thereby reducing the likelihood of an individual polymer SC being present in the solution. Consequently, this phenomenon slows the further increase in the conductivity.

According to Table 2, the degree of substitution (DS) represents the quantity of stearoyl embedded in the chitosan backbone. In addition, the increased stearoyl content led to higher DS values. The acylation procedure, conducted at a

**Table 2.** Estimation of Average Molecular Weight, Degree of Substitution, and SC Yield

	average molecular weight ( $M_w$ ) (kDa)	degree of substitution (DS)	yield (%)	crystallinity index (%)	solubility in DI water at 30 °C ( $\text{g}\cdot\text{L}^{-1}$ )	CMC ( $\text{mg}\cdot\text{mL}^{-1}$ )
NC	17		67		$5.84 \pm 0.01$	$0.88 \pm 0.01$
SC1	27	0.15	88	98.5	$1.93 \pm 0.05$	$0.07 \pm 0.02$
SC2	29	0.17	73	97.7	$1.60 \pm 0.03$	$0.06 \pm 0.02$
SC3	41	0.29	87	99.2	$1.20 \pm 0.03$	$0.05 \pm 0.07$
SC4	49	0.33	78	99.0	$0.51 \pm 0.02$	$0.04 \pm 0.02$
SC5	57	0.47	81	94.8	$0.11 \pm 0.01$	$0.02 \pm 0.01$

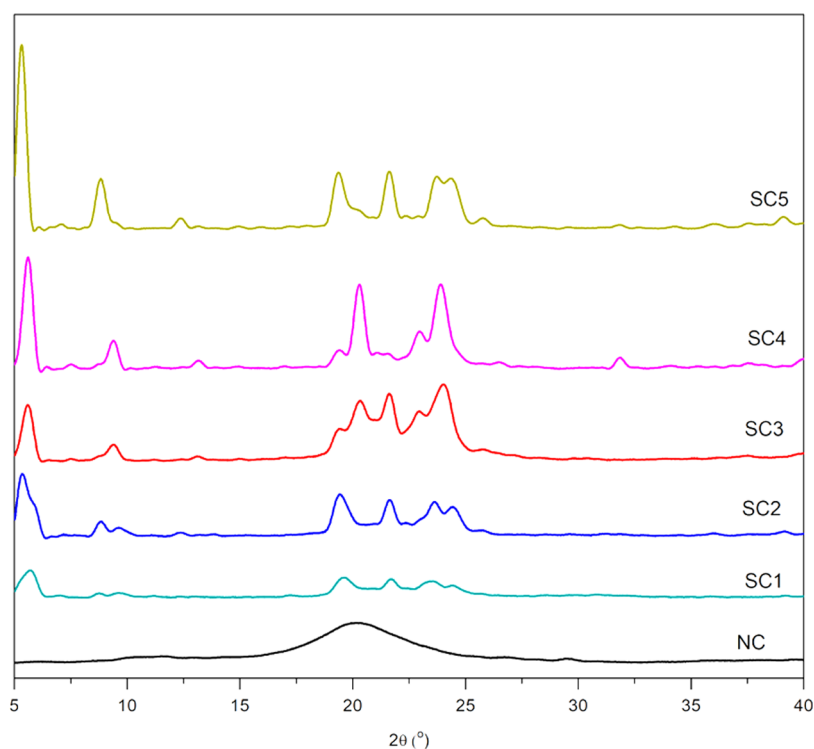


Figure 5. XRD patterns of NC and various SCs.

temperature of 30 °C, yielded a product with a purity of over 70%. This indicated the successful substitution of the hydrogen atom attached to the amino group with an acyl group. In addition, the findings suggest that the acylation process can be feasibly performed at ambient temperature.

**3.4. XRD Analysis.** Figure 5 shows the XRD patterns of the NC and various SCs. The diffractogram of NC displayed broad peaks at  $2\theta = 20.4$  and  $10.4^\circ$ , attributed to amine I ( $-\text{N}-\text{CO}-\text{CH}_3$ ) of chitosan and amine II ( $-\text{NH}_2$ ) of chitosan, respectively. The peak near  $20^\circ$  became broader and weaker, indicating an amorphous state of their crystalline structures and a substantial reduction of intramolecular hydrogen bonds.<sup>50</sup> The diffractogram of NC displayed broad peaks at  $2\theta = 20.4$  and  $10.4^\circ$ , which signified its amorphous characteristics.<sup>51</sup> The introduction of a stearyl group into the chitosan backbone significantly altered its structure and enhanced its crystallinity. It can be observed from the X-ray patterns of SC that the strongest reflections appeared at about  $2\theta = 5.5^\circ$  and at about  $19\text{--}25^\circ$ , which corresponds to a stearyl group. Moreover, several weak peaks at  $2\theta = 8, 13,$  and  $32^\circ$  probably correspond to highly ordered long alkyl chains. The crystallinity percentage was calculated using the equation below<sup>52</sup>

$$\% \text{crystalline} = \frac{I_{002} - I_{\text{am}}}{I_{002}} \times 100 \quad (9)$$

where  $I_{002}$  refers to the maximum intensity of the (002) lattice diffraction and  $I_{\text{am}}$  represents the diffraction intensity at  $2\theta = 20.4^\circ$ .

Both SC3 and SC4 exhibited the highest crystallinity index, which was ascribed to the well-arranged stearyl chains and possible hydrophobic interactions within their structures. The increment of DS in SC distorted the stearyl group, which lowered the crystallinity index.

**3.5. Particle Size and  $\zeta$ -Potential.** As shown in Figure 6a, a significant increase was noted in the particle size of NC, which ranged from  $74 \pm 17$  to  $170 \pm 24$  nm with an increase in concentration between 0.008 and 0.04%. This outcome was ascribed to the increasing concentration, which led to a larger particle size as a result of self-assembly. The other SC nanoparticles displayed a similar trend in which the particle size increased progressively with increasing DS. The findings revealed various polydispersity indices for both the NC and SC particles, which reflected the distribution of large-sized particles. Figure 6a depicts the correlation between the particle sizes of various SCs and the differences in their concentrations in aqueous solution. The depolymerization of chitosan, denoted as NC, resulted in a reduction in particle size from  $170 \pm 24$  to  $74 \pm 17$  nm, following five consecutive dissolution cycles. A similar pattern was noted in SC5, but the observed change was relatively less substantial in comparison of SC1–SC4. This dilution leads to a decrease in the number of particles present, resulting in a diminished likelihood of collisions or interactions between the particles. Ultimately, Brownian motion decelerates, leading to a reduction in light scattering, as indicated by the diminishing size of the SC particles. Additionally, Figure 6a demonstrates a noticeable correlation between the ratio of stearyl incorporated into chitosan and the resulting particle size. The relationship between the ratio of stearyl to chitosan (SC5) and particle size can be easily understood because an increase in the stearyl ratio results in a reduction in particle size. As the amount of stearyl rises, the van der Waals forces increase, resulting in a more pronounced attraction among the polymer chains, thereby facilitating their closer proximity. Consequently, this phenomenon led to a reduction in the particle size.

The polydispersity index (PDI) in Figure 6b illustrates the particle size distributions of both the NC and SC. Among

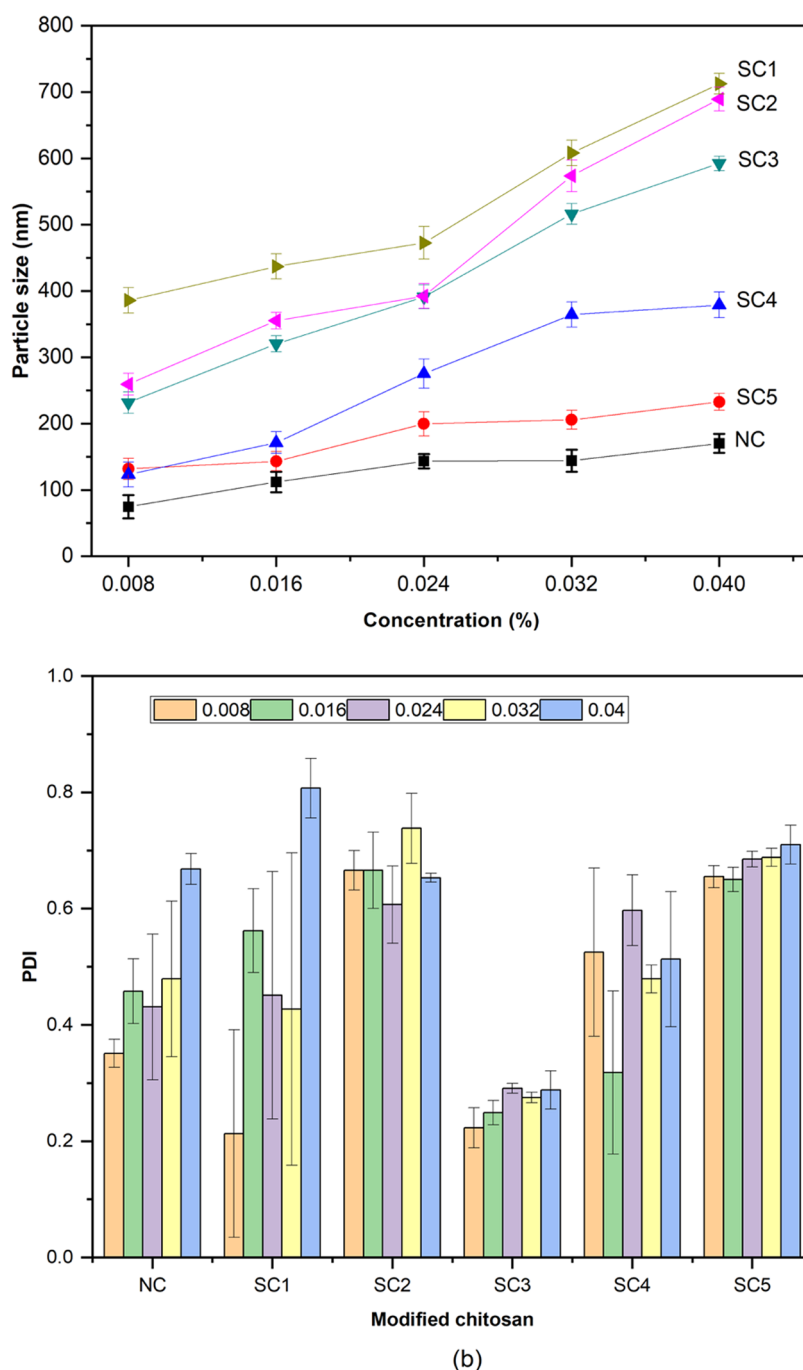


**Figure 6.** DLS measurements of NC, SC1, SC2, SC3, SC4, and SC5: (a) particle size and (b) PDI.

them, SC1 exhibited the widest PDI values, ranging from 0.23 to 0.81. This phenomenon might be attributed to the relatively low concentration of stearyl groups attached to chitosan. As a result, SC1 exhibits a preference for integration within an aqueous solution rather than for particle formation. Consequently, the particle size distribution of SC1 was nonuniform. In contrast to the situation observed in SC3, the PDI value exhibited a very consistent trend within the range of 0.22–0.28 across five different concentrations. This finding demonstrates that the formulation denoted as SC3 exhibits superior stability in terms of particle size dispersion. In the pharmaceutical industry, a PDI value of less than 0.3 is critical for assessing the durability of colloid dosage forms during storage. Formulating encapsulated therapeutic drugs requires

careful consideration of the size distribution of drug delivery systems throughout time.<sup>53</sup>

$\zeta$ -Potential measurements were performed in this experimental study to determine the stability of the SC nanoparticles as a colloidal system in an aqueous solution, as shown in Figure 7. The positive  $\zeta$ -potential value exhibited by NC can be attributed to the presence of an amine group that carries a positive charge. The stability of this depolymerized chitosan with respect to its  $\zeta$ -potential was shown to be generally consistent within the concentration range 0.008–0.032%, exhibiting an average value of approximately 5 mV. However, it is notable that at the highest concentration, a slight drop in the  $\zeta$ -potential was observed, potentially indicating the initiation of aggregation or the occurrence of strong particle

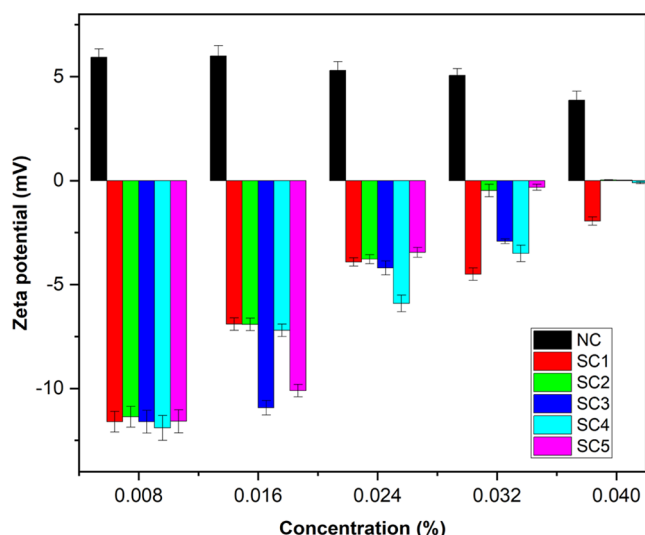


Figure 7.  $\zeta$ -Potentials of NC, SC1, SC2, SC3, SC4, and SC5.

interactions. In addition, the introduction of stearyl to the amine group subsequent to the acylation procedure resulted in the modification of the  $\zeta$ -potential, rendering it a negative value. This indicated that the acylation of chitosan decreased the  $\zeta$ -potential. The  $\zeta$ -potential value of  $\sim 0$  mV indicated that the systems preferred aggregation at larger concentrations of both NC and SC. The aggregation of particles results in a reduction in the repulsive forces acting between them, causing a drop in the value of the  $\zeta$ -potential. Among the five ratios of stearyl/chitosan, SC3 and SC5 exhibited  $\zeta$ -potential values above  $-10$  mV at the two lowest concentrations. This indicated that these two stearyl chitosan compounds demonstrated considerable stability when dissolved in an aqueous medium.

Dynamic light scattering (DLS) studies revealed that SC3 exhibited the most favorable system stability, as evidenced by its superior performance in terms of the average particle size, PDI value, and  $\zeta$ -potential. Consequently, SC3 was selected as the carrier for the three antimetabolites with varying  $\log P$  values. The concurrent use of the three antimetabolites resulted in alterations in the mean particle size, polydispersity index (PDI), and  $\zeta$ -potential, as shown in Table 3.

Table 3. Particle Size, PDI, and  $\zeta$ -Potential of SC3 and Drug-Loaded SC3

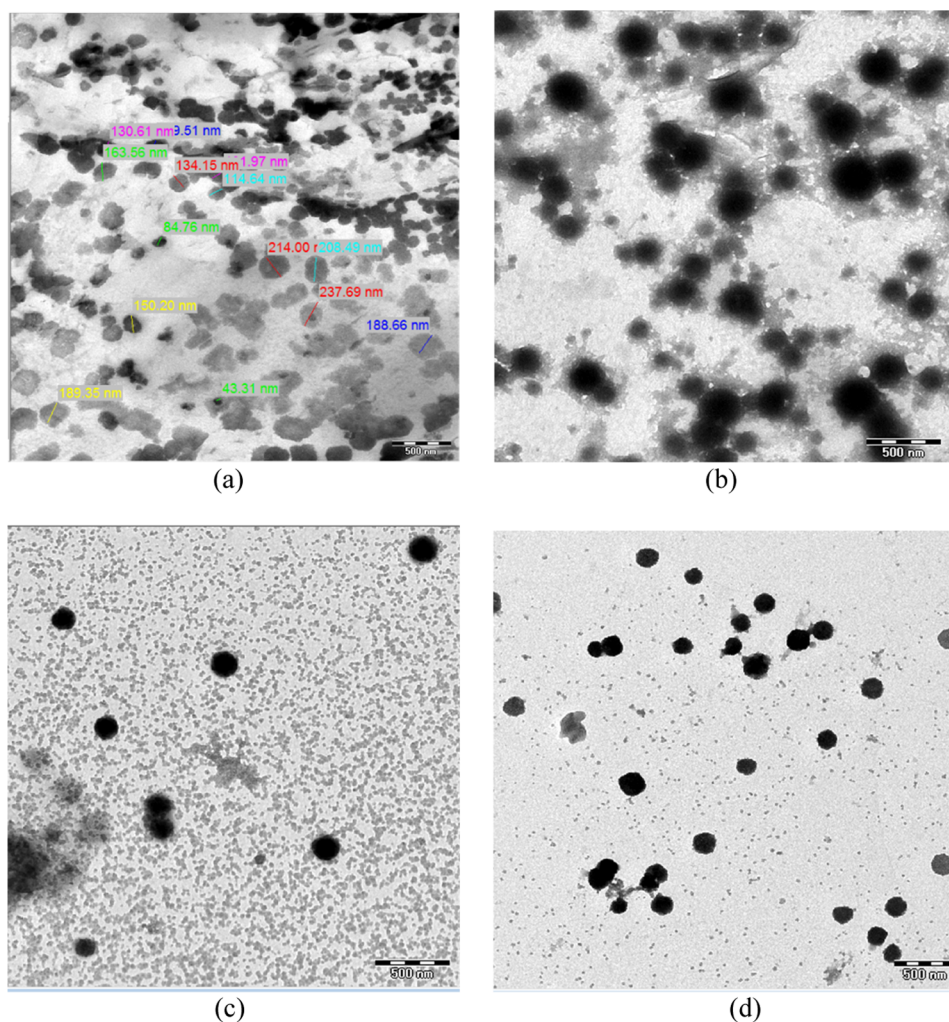
sample	particle size (nm)		PDI (DLS)	$\zeta$ -potential (mV)
	DLS measurement	TEM micrograph		
drug-free SC3	320 $\pm$ 12	155 $\pm$ 15	0.25 $\pm$ 0.02	-10.93 $\pm$ 0.35
P-SC3	687 $\pm$ 28	369 $\pm$ 22	0.59 $\pm$ 0.08	-7.25 $\pm$ 1.31
M-SC3	502 $\pm$ 13	277 $\pm$ 18	0.69 $\pm$ 0.18	-9.64 $\pm$ 1.15
R-SC3	582 $\pm$ 65	225 $\pm$ 12	0.59 $\pm$ 0.16	-15.93 $\pm$ 0.72

Table 3 shows that the average particle size obtained from DLS measurements was greater than that observed in the transmission electron microscopy (TEM) images for all samples. This phenomenon can be attributed to the utilization of the DLS technique, wherein the particles are distributed within an aqueous solution. Consequently, the dimensions of the particles are influenced by the presence of the surrounding

liquid layer. In TEM, the examination was conducted under vacuum, and the particles were in a desiccated state, ensuring that the resulting size measurement was predominantly representative of the particle size. When examining the PDI values associated with the three antimetabolites loaded into SC3, it was observed that these values were within the range of 0.5, suggesting a relatively broad particle size distribution. On the other hand, the SC3 formulation loaded with raltitrexed had the highest  $\zeta$ -potential value of  $-15.93$ . The observed phenomenon can be attributed to the relatively lower logarithmic partition coefficient ( $\log P$ ) of raltitrexed compared to pemetrexed and methotrexate. This indicated that raltitrexed exhibited a reduced affinity for hydrophobic interactions with the stearyl group, favoring attachment or interaction through the formation of hydrogen bonds with the hydrophilic group on SC3. In contrast, the  $\zeta$ -potential of SC3 decreased after loading pemetrexed. This decrease can be attributed to the hydrophobic nature of pemetrexed, which induces the formation of intermolecular forces with the nonpolar groups present on SC3.

**3.6. Morphology Analysis.** The limited contrast observed under transmission electron microscopy (TEM) can be attributed to the electron sensitivity of TEM images and the low atomic number ( $Z$ ) of the chitosan backbone, which mostly comprises carbon, hydrogen, nitrogen, and oxygen atoms. Based on previous characterization, SC3 was selected as the carrier in this experimental study to be amalgamated with drugs because of its ideal particle size and stability as a drug delivery system. The TEM images revealed that drug-loaded SC3 exhibited a predominantly spherical morphology, albeit with variations in size. Figure 8a illustrates that the average particle size of SC3 was 160 nm, representing a reduction of 50% compared to the particle size obtained from dynamic light scattering (DLS) measurements. This phenomenon can be observed in dynamic light scattering (DLS) analysis, where the particle size is determined based on the hydrodynamic radius of all particles in the sample following solvent penetration, encompassing both individual particles and those that have formed aggregates. Transmission electron microscopy (TEM) provides insights into the dimensional characteristics of particles in the dry state. As depicted in Figure 8b–d, the spherical morphology of stearyl chitosan remained unchanged after incorporation of the three antimetabolites possessing distinct  $\log P$ . Upon comparing drug-free SC3 with the three drug-loaded SCs, it was observed that the particle size increased, particularly in the case of pemetrexed. This phenomenon was facilitated by pemetrexed, which exhibited a positive  $\log P$ . This indicates that the hydrophobic moiety of pemetrexed has a greater affinity for binding to the hydrophobic stearyl chain than methotrexate and raltitrexed. Meanwhile, the size of methotrexate- and raltitrexed-loaded SC particles increased slightly compared to drug-free SC. Based on these images and the average particle size, it was possible to determine the position of the antimetabolite-incorporated SC. Specifically, it can be inferred that pemetrexed could be located within the inner nonpolar stearyl group of chitosan. Methotrexate and raltitrexed, however, most likely reside around the hydrophilic regions of the SC. Furthermore, both antimetabolites exhibited a negative  $\log P$  value, which indicates a stronger affinity for the aqueous phase.

**3.7. Encapsulation Efficiency and Drug Loading.** The encapsulation efficiencies and drug-loading capacities of SC3 are listed in Table 4. Notably, the drug loading of all



**Figure 8.** TEM image of (a) SC3, (b) pemetrexed-loaded SC3, (c) methotrexate-loaded SC3, and (d) raltitrexed-loaded SC3.

**Table 4. Drug Loading and Encapsulation Efficiency**

weight ratio SC-3: drug	drug loading (%)			encapsulation efficiency (%)		
	P	M	R	P	M	R
1:0.025	6.8 ± 2.0	2.4 ± 0.2	2.1 ± 1.3	93.6 ± 1.6	94.5 ± 1.4	94.3 ± 1.2
1:0.05	17.0 ± 3.8	4.6 ± 0.1	4.6 ± 0.2	92.0 ± 3.4	92.8 ± 1.4	92.0 ± 1.2
1:0.075	26.1 ± 2.4	6.9 ± 0.2	6.9 ± 3.0	89.9 ± 2.5	92.3 ± 1.2	92.5 ± 2.2
1:0.1	36.8 ± 1.1	9.1 ± 0.3	9.2 ± 2.1	85.1 ± 3.5	92.1 ± 2.4	92.4 ± 3.0
1:0.125	46.7 ± 1.4	11.6 ± 0.3	11.8 ± 1.3	69.5 ± 2.8	91.8 ± 2.7	86.2 ± 3.5

antimetabolites increased with the amount of drug incorporated into SC nanoparticles. Pemetrexed had the largest drug-loading value, approximately three times those of methotrexate and raltitrexed. This was made feasible by the extensive van der Waals forces between the benzene of pemetrexed and stearyl, allowing more pemetrexed loading into the SC. In contrast, for methotrexate and raltitrexed, the presence of nitrogen and sulfur atoms in the middle of these structures weakened the van der Waals interactions. Hence, both drugs attained low drug loading values.

As shown in Table 4, the encapsulation efficiency of the three drugs ranged from 93.6 to 94.5% at low drug weights. Nonetheless, the encapsulation efficiency demonstrated by pemetrexed decreased steadily with increasing drug loading, stemming from the high amount of pemetrexed that was not tolerated by the SC and hindered the carrier–drug bond

formation. However, this phenomenon was absent in methotrexate and raltitrexed, attributable to the dipole–dipole interactions that occurred between the drugs encapsulated in the SC. In addition, both nitrogen and sulfur atoms cause partial charge in the molecules. Thus, the addition of the drug led to a stronger bonding force. This dismissed any correlation between the drug amount and encapsulation efficiency. Moreover, the encapsulation efficiency experienced a slight change because of the possibility of the drug being entrapped not only within the inner core, where stearyl exists, but also potentially attached to the hydrophilic region of SC3 facing outward. This, in turn, contributes to the attainment of a high encapsulation efficiency.

**3.8. In Vitro Drug Release.** Figure 9 illustrates the rate of drug release from the three selected antimetabolites for over 24 h with and without a carrier. The outcomes revealed that free

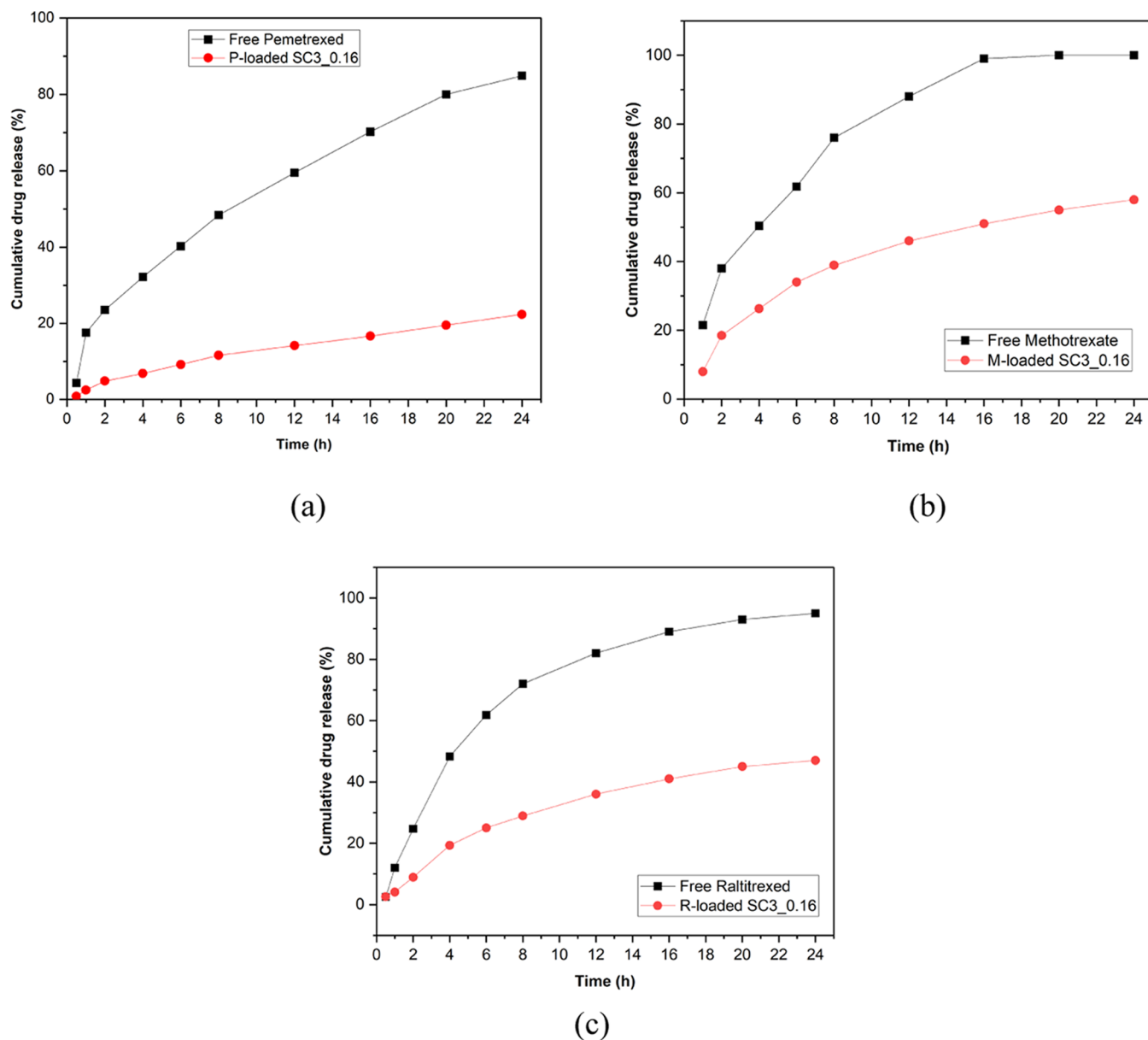


**Figure 9.** Cumulative release of free drug and drug-loaded SC3 at 0.016% concentrations: (a) pemetrexed, (b) methotrexate, and (c) raltitrexed.

**Table 5. Kinetic Model of Drug Release**

	zero-order	first order	higuchi	Korsmeyer-Peppas
P-loaded SC3	$R^2 = 0.9135$ $k_0 = 3.429$	$R^2 = 0.9887$ $k_1 = 0.055$	$R^2 = 0.9614$ $k_H = 13.820$	$R^2 = 0.9968$ $k_{KP} = 8.934$ $n = 0.665$
M-loaded SC3	$R^2 = 0.9302$ $k_0 = 1.151$	$R^2 = 0.9574$ $k_1 = 0.013$	$R^2 = 0.9513$ $k_H = 4.620$	$R^2 = 0.9963$ $k_{KP} = 2.773$ $n = 0.692$
R-loaded SC3	$R^2 = 0.9334$ $k_0 = 1.137$	$R^2 = 0.9598$ $k_1 = 0.013$	$R^2 = 0.9506$ $k_H = 4.561$	$R^2 = 0.9972$ $k_{KP} = 2.707$ $n = 0.697$

methotrexate was completely released within 16 h, while free pemetrexed and free raltitrexed were discharged to 80, and 95%, respectively, within 24 h. However, the incorporation of the three drugs into the SC drastically altered the drug release rate. It was found that about 20% of pemetrexed was released within 24 h, which displayed a significantly lower rate than

those of methotrexate and raltitrexed. In contrast, methotrexate release peaked at 60% and raltitrexed at approximately 40% within the same time frame. The diffusion of pemetrexed from the SC into the water-based medium occurred very slowly because of the strong bond formed between the drug molecule and the carrier. The aromatic part of pemetrexed could have

interacted with the nonpolar stearyl group through van der Waals force.<sup>54</sup> When the SC began to swell owing to the effect of temperature, pemetrexed required additional time to break the strong bond and diffuse into the medium.

It is noteworthy that a mathematical approach is applicable for comparing the cumulative release of drug models from the SC carrier. As tabulated in Table 5, among the three mathematical models used for comparative analysis with the retrieved experimental outcomes, the Korsmeyer–Peppas kinetic model displayed the best fit for modeling the in vitro drug release mechanism for all drugs loaded in the SC. As shown in Table 5, the kinetic studies showed that the cumulative drug release for the drug models was consistent with the Korsmeyer–Peppas kinetic model, whereby the  $R^2$  values retrieved for pemetrexed, methotrexate, and raltitrexed were 0.9968, 0.9963, and 0.9972, respectively. The release exponent ( $n$ ), which ranged from 0.665 to 0.697, revealed the mechanism of drug release via anomalous transport (non-Fickian diffusion).<sup>55</sup> Furthermore, the concentration gradient had no impact on the diffusion of the drug into the medium. Other factors (e.g., drug–carrier chemical interactions, swelling, and drug–diffusion medium interactions) affected the results.<sup>56</sup> Hence, SC has been proven in this study to offer an exceptional controlled release for all three tested antimetabolites.

#### 4. CONCLUSIONS

The hydrophobicity of chitosan improved after its acylation with stearyl, as evidenced by the validation of its structure by FTIR, <sup>1</sup>H NMR, and XRD analyses. The acylation process exhibited selectivity for the amine group, wherein stearyl preferentially binds to the amine nitrogen, resulting in the formation of an amide. The calculated crystallinity of stearyl chitosan exceeded 90%, suggesting an enhancement of its crystalline structure. The observed increase can be attributed to the proportional change in the weight ratio of chitosan to stearyl chloride, which affected the average molecular weight and degree of substitution. On the other hand, a notable decline in the solubility of SC in deionized water was noticed with values decreasing from 5.84 to 0.11 g·L<sup>-1</sup>. To minimize contact with the aqueous phase, SC, which is incorporated into the aqueous phase, starts to form aggregates at concentrations where SC conductivity measurements give CMC values between 0.02 and 0.07 mg·mL<sup>-1</sup>. Dynamic light scattering (DLS) observations revealed a correlation between the concentration of dispersed SC and the particle size. Specifically, the dilution of the SC solution leads to a decrease in the intensity of light scattering, resulting in a reduction in particle size. Among the five synthesized SCs, SC3 exhibited notable stability, as evidenced by its polydispersity index (PDI) values ranging from 0.22 to 0.28 and  $\zeta$ -potential exceeding -10 mV at low concentrations. The particle sizes of P-loaded SC3, M-loaded SC3, and R-loaded SC3 were 687, 502, and 582 nm, respectively, owing to the presence of the three antimetabolites. Raltitrexed-loaded SC3 had a  $\zeta$ -potential value of -15.93 mV, suggesting the presence of a significant repulsive force that enabled its stability in aqueous solution. Pemetrexed had the highest drug-loading capacity, although the encapsulation efficiency values for the three antimetabolites were quite similar. An in vitro release study showed that the release of the three drugs could be controlled within 24 h by incorporation into SC3 to improve the therapeutic efficiency.

#### ■ ASSOCIATED CONTENT

##### Supporting Information

The Supporting Information is available free of charge at <https://pubs.acs.org/doi/10.1021/acsomega.3c05108>.

Antimetabolite information and characterization data of stearyl chitosan as well as antimetabolite-incorporated SC (PDF)

#### ■ AUTHOR INFORMATION

##### Corresponding Author

Anita Marlina – Research Centre for Chemistry, National Research and Innovation Agency Republic of Indonesia, South Tangerang 15314, Indonesia; Department of Chemistry, Faculty of Science, University of Malaya, Kuala Lumpur 50603, Malaysia; [orcid.org/0000-0002-8802-3746](https://orcid.org/0000-0002-8802-3746); Email: [anita.marlina@brin.go.id](mailto:anita.marlina@brin.go.id)

##### Author

Misni Misran – Department of Chemistry, Faculty of Science, University of Malaya, Kuala Lumpur 50603, Malaysia

Complete contact information is available at:

<https://pubs.acs.org/10.1021/acsomega.3c05108>

##### Notes

The authors declare no competing financial interest.

#### ■ ACKNOWLEDGMENTS

This study was funded by the Malaysian Ministry of Higher Education (FRGS/1/2018/STG07/UM/01/1).

#### ■ REFERENCES

- (1) Valencia-Lazcano, A. A.; Hassan, D.; Pourmadadi, M.; Shamsabadipour, A.; Behzadmehr, R.; Rahdar, A.; Medina, D. I.; Diez-Pascual, A. M. 5-Fluorouracil nano-delivery systems as a cutting-edge for cancer therapy. *Eur. J. Med. Chem.* **2023**, *246*, No. 114995.
- (2) Yadav, A.; Singh, S.; Sohi, H.; Dang, S. Advances in Delivery of Chemotherapeutic Agents for Cancer Treatment. *AAPS PharmSciTech* **2022**, *23* (1), No. 25, DOI: [10.1208/s12249-021-02174-9](https://doi.org/10.1208/s12249-021-02174-9).
- (3) Barnett, C.; Joubert, F.; Iliopoulou, A.; Álvarez, R. S.; Pasparakis, G. Photochemical Internalization Using Natural Anticancer Drugs, Antimetabolites, and Nanoformulations: A Systematic Study against Breast and Pancreatic Cancer Cell Lines. *Mol. Pharmaceut.* **2023**, *20* (3), 1818–1841.
- (4) Hrubá, L.; Das, V.; Hajdúch, M.; Dzubak, P. Nucleoside-based anticancer drugs: Mechanism of action and drug resistance. *Biochem. Pharmacol.* **2023**, *215*, No. 115741.
- (5) Al Saihati, H. A.; Rabaan, A. A. Cellular resistance mechanisms in cancer and the new approaches to overcome resistance mechanisms chemotherapy. *Saudi Med. J.* **2023**, *44* (4), 329–344.
- (6) Alzahrani, S. M.; Al Doghaither, H. A.; Al-Ghafari, A. B.; Pushparaj, P. N. 5-Fluorouracil and capecitabine therapies for the treatment of colorectal cancer (Review). *Oncol. Rep.* **2023**, *50* (4), No. 175, DOI: [10.3892/or.2023.8612](https://doi.org/10.3892/or.2023.8612).
- (7) Shakerzadeh, E. Efficient carriers for anticancer 5-fluorouracil drug based on the bare and M-encapsulated (M = Na and Ca) B40 fullerenes; in silico investigation. *J. Mol. Liq.* **2021**, *343*, No. 116970.
- (8) Alexandrovich, T. P.; Khan, A. Molecular insights into the encapsulation of fluorouracil molecule inside the single-walled carbon nanotubes. *Diamond Relat. Mater.* **2022**, *124*, No. 108900.
- (9) Sheng, Y.; Beguin, E.; Nesbitt, H.; Kamila, S.; Owen, J.; Barnsley, L. C.; Callan, B.; O’Kane, C.; Nomikou, N.; Hamoudi, R.; Taylor, M. A.; Love, M.; Kelly, P.; O’Rourke, D.; Stride, E.; McHale, A. P.; Callan, J. F. Magnetically responsive microbubbles as delivery vehicles for targeted sonodynamic and antimetabolite therapy of pancreatic cancer. *J. Controlled Release* **2017**, *262*, 192–200.

- (10) Mohd-Zahid, M. H.; Mohamud, R.; Abdullah, C. A. C.; Lim, J.; Alem, H.; Hanaffi, W. N. W.; Iskandar, Z. A. Colorectal cancer stem cells: a review of targeted drug delivery by gold nanoparticles. *RSC Adv.* **2020**, *10* (2), 973–985, DOI: 10.1039/C9RA08192E.
- (11) Vakilinezhad, M. A.; Amini, A.; Dara, T.; Alipour, S. Methotrexate and Curcumin co-encapsulated PLGA nanoparticles as a potential breast cancer therapeutic system: In vitro and in vivo evaluation. *Colloids Surf. B* **2019**, *184*, No. 110515.
- (12) Bernabeu, E.; Gonzalez, L.; Cagel, M.; Moretton, M. A.; Chiappetta, D. A. Deoxycholate-TPGS mixed nanomicelles for encapsulation of methotrexate with enhanced in vitro cytotoxicity on breast cancer cell lines. *J. Drug Delivery Sci. Technol.* **2019**, *50*, 293–304.
- (13) Li, X.; Liang, C.; Guo, Y.; Su, J.; Chen, X.; Macgregor, R. B.; Zhang, R. X.; Yan, H. Clinical Translation of Long-Acting Drug Delivery Systems for Posterior Capsule Opacification Prophylaxis. *Pharmaceutics* **2023**, *15*, No. 1235, DOI: 10.3390/pharmaceutics15041235.
- (14) Lima, R.; Fernandes, C.; Pinto, M. M. M. Molecular modifications, biological activities, and applications of chitosan and derivatives: A recent update. *Chirality* **2022**, *34*, 1166–1190, DOI: 10.1002/chir.23477.
- (15) Gao, Y.; Wu, Y. Recent advances of chitosan-based nanoparticles for biomedical and biotechnological applications. *Int. J. Biol. Macromol.* **2022**, *203*, 379–388.
- (16) Rahimi, M.; Mir, S. M.; Baghban, R.; Charmi, G.; Plummer, C. M.; Shafiei-Irannejad, V.; Soleymani, J.; Pietrasik, J. Chitosan-based biomaterials for the treatment of bone disorders. *Int. J. Bio. Macromol.* **2022**, *215*, 346–367.
- (17) Mohanbhai, S. J.; Sardoiwala, M. N.; Gupta, S.; Shrimali, N.; Choudhury, S. R.; Sharma, S. S.; Guchhait, P.; Karmakar, S. Colon targeted chitosan-melatonin nanotherapy for preclinical Inflammatory Bowel Disease. *Biomater. Adv.* **2022**, *136*, No. 212796.
- (18) Lohiya, G.; Katti, D. S. Carboxylated chitosan-mediated improved efficacy of mesoporous silica nanoparticle-based targeted drug delivery system for breast cancer therapy. *Carbohydr. Polym.* **2022**, *277*, No. 118822.
- (19) Sahatsapan, N.; Pamornpathomkul, B.; Rojanarata, T.; Ngawhirunpat, T.; Poonkhum, R.; Opanasopit, P.; Patrojanasophon, P. Feasibility of mucoadhesive chitosan maleimide-coated liposomes for improved buccal delivery of a protein drug. *J. Drug Delivery Sci. Technol.* **2022**, *69*, No. 103173.
- (20) Baharlouei, P.; Rahman, A. Chitin and Chitosan: Prospective Biomedical Applications in Drug Delivery, Cancer Treatment, and Wound Healing. *Mar. Drugs* **2022**, *20*, No. 460, DOI: 10.3390/md20070460.
- (21) Tiew, S. X.; Misran, M. Encapsulation of salicylic acid in acylated low molecular weight chitosan for sustained release topical application. *J. Appl. Polym. Sci.* **2017**, *134* (36), No. 44849, DOI: 10.1002/app.45273.
- (22) Lu, B.; Lv, X.; Le, Y. Chitosan-Modified PLGA Nanoparticles for Control-Released Drug Delivery. *Polymers* **2019**, *11*, No. 304, DOI: 10.3390/polym11020304.
- (23) Ahmad, S.; Khan, I.; Pandit, J.; Emad, N. A.; Bano, S.; Dar, K. I.; Rizvi, M. M. A.; Ansari, M. D.; Aqil, M.; Sultana, Y. Brain targeted delivery of carmustine using chitosan coated nanoparticles via nasal route for glioblastoma treatment. *Int. J. Bio. Macromol.* **2022**, *221*, 435–445.
- (24) Ramadan, I.; Nassar, M. Y.; Gomaa, A. In-vitro Investigation of the Anticancer Efficacy of Carboplatin-Loaded Chitosan Nanocomposites Against Breast and Liver Cancer Cell Lines. *J. Polym. Environ.* **2022**, 1102–1115, DOI: 10.1007/s10924-022-02668-y.
- (25) Reis, B.; Gerlach, N.; Steinbach, C.; Carrasco, K. H.; Oelmann, M.; Schwarz, S.; Müller, M.; Schwarz, D. A Complementary and Revised View on the N-Acylation of Chitosan with Hexanoyl Chloride. *Mar. Drugs* **2021**, *19* (7), No. 385, DOI: 10.3390/md19070385.
- (26) Eh Suk, V. R.; Marlina, A.; Hussain, Z.; Misran, M. N-Stearoyl Chitosan as a Coating Material for Liposomes Encapsulating Itraconazole. *Arab. J. Sci. Eng.* **2021**, *46* (6), 5645–5653.
- (27) Zhu, B.; Shi, J.; Sun, H.; Xia, L.; Fang, W.; Li, H.; Liu, W.; Han, B. Butyryl chitosan: Synthesis, characterization and evaluation of the sustained release performance as tacrolimus carrier. *Chem. Eng. J.* **2022**, *446*, No. 136743.
- (28) Chirio, D.; Peira, E.; Sapino, S.; Dianzani, C.; Barge, A.; Muntoni, E.; Morel, S.; Gallarate, M. Stearoyl-Chitosan Coated Nanoparticles Obtained by Microemulsion Cold Dilution Technique. *Int. J. Mol. Sci.* **2018**, *19* (12), No. 3833, DOI: 10.3390/ijms19123833.
- (29) Chatterjee, S.; Judeh, Z. M. A. Encapsulation of fish oil with N-stearoyl O-butylglyceryl chitosan using membrane and ultrasonic emulsification processes. *Carbohydr. Polym.* **2015**, *123*, 432–442.
- (30) Liu, Z.; Zhang, T.; Tang, C.; Yin, C. Amphiphilic nanoparticles based on poly(vinyl pyrrolidone) and stearoyl modified chitosan as drug vehicles for paclitaxel delivery. *Mater. Lett.* **2016**, *185*, 226–229.
- (31) Yang, T.; Feng, J.; Zhang, Q.; Wu, W.; Mo, H.; Huang, L.; Zhang, W. l-Carnitine conjugated chitosan-stearic acid polymeric micelles for improving the oral bioavailability of paclitaxel. *Drug Delivery* **2020**, *27* (1), 575–584.
- (32) Ahangaran, F. Microencapsulation: Solvent evaporation *Principles of Biomaterials Encapsulation: Volume One*; WP, 2023; Chapter 18, pp 377–392.
- (33) Bharate, S. S.; Kumar, V.; Vishwakarma, R. A. Determining Partition Coefficient (Log P), Distribution Coefficient (Log D) and Ionization Constant (pKa) in Early Drug Discovery. *Comb. Chem. High Throughput Screening* **2016**, *19* (6), 461–469, DOI: 10.2174/1386207319666160502123917.
- (34) Rosch, J. G.; DuRoss, A. N.; Landry, M. R.; Sun, C. Development of a Pemetrexed/Folic Acid Nanoformulation: Synthesis, Characterization, and Efficacy in a Murine Colorectal Cancer Model. *ACS Omega* **2020**, *5* (25), 15424–15432.
- (35) Rui, Q.; Gao, J.; Yin, Z.-Z.; Li, J.; Cai, W.; Wu, D.; Kong, Y. A biodegradable pH and glutathione dual-triggered drug delivery system based on mesoporous silica, carboxymethyl chitosan and oxidized pullulan. *Int. J. Bio. Macromol.* **2023**, *224*, 1294–1302.
- (36) Wang, H.; Shao, W.; Lu, X.; Gao, C.; Fang, L.; Yang, X.; Zhu, P. Synthesis, characterization, and in vitro anti-tumor activity studies of the hyaluronic acid-mangiferin-methotrexate nanodrug targeted delivery system. *Int. J. Bio. Macromol.* **2023**, *239*, No. 124208.
- (37) Zhao, W.; Zheng, L.; Yang, J.; Ma, Z.; Tao, X.; Wang, Q. Dissolving microneedle patch-assisted transdermal delivery of methotrexate improve the therapeutic efficacy of rheumatoid arthritis. *Drug Delivery* **2023**, *30* (1), 121–132.
- (38) Morey, J.; Llinás, P.; Bueno-Costa, A.; León, A. J.; Piña, M. N. Raltitrexed-Modified Gold and Silver Nanoparticles for Targeted Cancer Therapy: Cytotoxicity Behavior In Vitro on A549 and HCT-116 Human Cancer Cells. *Materials* **2021**, *14* (3), No. 534, DOI: 10.3390/ma14030534.
- (39) Bi, Y.; Wang, Y.; Zhang, W.; Lu, H.; Ren, J.; Han, X. Preliminary outcomes of DEB-TACE loaded with raltitrexed in the treatment of unresectable or recurrent hepatocellular carcinoma. *Cancer Imaging* **2023**, *23* (1), No. 19, DOI: 10.1186/s40644-023-00534-1.
- (40) Sajid, A.; Castronovo, M.; Goycoolea, F. M. On the Fractionation and Physicochemical Characterisation of Self-Assembled Chitosan–DNA Polyelectrolyte Complexes. *Polymers* **2023**, No. 2115, DOI: 10.3390/polym15092115.
- (41) Muthamma, K.; Sunil, D.; Shetty, P.; Kulkarni, S. D.; Wagle, S.; Alex, A. T. Modified chitosan as a multi-functional material in eco-friendly formulation for anti-counterfeit applications. *React. Funct. Polym.* **2023**, *188*, No. 105603.
- (42) Amor, I. B.; Hemmami, H.; Laouini, S. E.; Abdelaziz, A. G.; Barhoum, A. Influence of chitosan source and degree of deacetylation on antibacterial activity and adsorption of AZO dye from water. *Biomass Convers. Biorefin.* **2023**, 1–11, DOI: 10.1007/s13399-023-03741-9.

- (43) Zhang, Y.; Huo, M.; Zhou, J.; Zou, A.; Li, W.; Yao, C.; Xie, S. DDSolver: an add-in program for modeling and comparison of drug dissolution profiles. *AAPS J.* **2010**, *12* (3), 263–271.
- (44) Nikonenko, N. A.; Buslov, D. K.; Sushko, N. I.; Zhibankov, R. G. Investigation of stretching vibrations of glycosidic linkages in disaccharides and polysaccharides with use of IR spectra deconvolution. *Biopolymers* **2000**, *57* (4), 257–262.
- (45) Eo, K.; Hwang, D.; Lee, K.; Kim, M.; Choi, K.; Kwon, Y. K. Nitrate permeability of semi-permeable membranes prepared from binary blends of cellulose triacetate and chitosan. *Polym. Eng. Sci.* **2018**, *58* (2), 192–197.
- (46) Piegat, A.; Goszczyńska, A.; Idzik, T.; Niemczyk, A. The Importance of Reaction Conditions on the Chemical Structure of N,O-Acylated Chitosan Derivatives. *Molecules* **2019**, *24* (17), No. 3047, DOI: [10.3390/molecules24173047](https://doi.org/10.3390/molecules24173047).
- (47) Hu, Y.; Du, Y.; Yang, J.; Tang, Y.; Li, J.; Wang, X. Self-aggregation and antibacterial activity of N-acylated chitosan. *Polymer* **2007**, *48* (11), 3098–3106.
- (48) Yan, T.; Feringa, B. L.; Barta, K. Direct N-alkylation of unprotected amino acids with alcohols. *Sci. Adv.* **2017**, *3* (12), No. eaao6494, DOI: [10.1126/sciadv.aao6494](https://doi.org/10.1126/sciadv.aao6494).
- (49) Azahar, S. S.; Hamidon, T. S.; Latip, A. F. A.; Hussin, M. H. Physicochemical and conductivity studies of chitosan-tapioca flour-LiBF<sub>4</sub> gel polymer electrolytes. *Chem. Phys. Impact* **2021**, *3*, No. 100055.
- (50) Zhu, B.; Shi, J.; Sun, H.; Xia, L.; Fang, W.; Li, H.; Liu, W.; Han, B. Butyryl chitosan: Synthesis, characterization and evaluation of the sustained release performance as tacrolimus carrier. *Chem. Eng. J.* **2022**, *446*, No. 136743, DOI: [10.1016/j.cej.2022.136743](https://doi.org/10.1016/j.cej.2022.136743).
- (51) Guan, Y.; Yu, C.; Zang, Z.; Wan, X.; Naeem, A.; Zhang, R.; Zhu, W. Chitosan/xanthan gum-based (Hydroxypropyl methylcellulose-co-2-Acrylamido-2-methylpropane sulfonic acid) interpenetrating hydrogels for controlled release of amorphous solid dispersion of bioactive constituents of *Pueraria lobata*. *Int. J. Bio. Macromol.* **2023**, *224*, 380–395.
- (52) Vydrina, I.; Malkov, A.; Vashukova, K.; Tyshkunova, I.; Mayer, L.; Faleva, A.; Shestakov, S.; Novozhilov, E.; Chukhchin, D. A new method for determination of lignocellulose crystallinity from XRD data using NMR calibration. *Carbohydr. Polym. Technol. Appl.* **2023**, *5*, No. 100305.
- (53) Danaei, M.; Dehghankhold, M.; Ataei, S.; Davarani, F. H.; Javanmard, R.; Dokhani, A.; Khorasani, S.; Mozafari, M. R. Impact of Particle Size and Polydispersity Index on the Clinical Applications of Lipidic Nanocarrier Systems. *Pharmaceutics* **2018**, *10* (2), No. 57, DOI: [10.3390/pharmaceutics10020057](https://doi.org/10.3390/pharmaceutics10020057).
- (54) Khalil, R. A.; Saadoon, F. A. Effect of presence of benzene ring in surfactant hydrophobic chain on the transformation towards one dimensional aggregate. *J. Saudi Chem. Soc.* **2015**, *19* (4), 423–428.
- (55) Ritger, P. L.; Peppas, N. A. A simple equation for description of solute release II. Fickian and anomalous release from swellable devices. *J. Controlled Release* **1987**, *5* (1), 37–42.
- (56) Fu, Y.; Kao, W. J. Drug release kinetics and transport mechanisms of non-degradable and degradable polymeric delivery systems. *Expert Opin. Drug Delivery* **2010**, *7* (4), 429–444.